CMS Physics Analysis Summary

Search for highly energetic double Higgs boson production in the two bottom quark and two vector boson all-hadronic final state

The CMS Collaboration

Abstract

A search for standard model (SM) nonresonant Higgs boson pair (HH) production is performed in the two bottom quark ($b\bar{b}$) and all-hadronic two vector boson (VV $\rightarrow$ 4q) final states. The search is carried out in proton-proton collisions at 13 TeV with a dataset corresponding to a total luminosity of $138\,\text{fb}^{-1}$. The analysis focuses on highly Lorentz-boosted HH candidates, where each Higgs boson's daughter quarks are all merged inside a single large radius jet. A new global particle transformer (GloParT) classifier is used to effectively perform boosted VV $\rightarrow$ 4q jet identification. The multiplicative modifier of the SM quartic coupling between two Higgs bosons and two vector bosons is observed (expected) to be constrained at 95% confidence level to $\kappa_{2V} \in [-0.04, 2.05]$ ($[0.05, 1.98]$).

1 Introduction

Since discovering the Higgs boson (H), a significant component of the CMS and ATLAS experiments' physics programs consists of precisely characterizing the new particle. This includes measuring properties such as its mass [1–3], width [4, 5], off-shell production [4, 5], and couplings to other standard model (SM) particles [6–8]. The measurement of the quartic HHVV coupling is particularly challenging, but one in which CMS has been making progress, largely through searches for highly Lorentz-boosted Higgs boson pair (HH) production.

HH production in the SM occurs dominantly through gluon fusion (ggF), with a small production cross section $\sigma_{\text{ggF}} = 31.05^{+2.2\%}_{-5.0\%} \pm 3\%(\text{PDF} + \alpha_{\text{S}})^{+4\%}_{-18\%}(m_{\text{t}})$ fb [9, 10] at a center of mass energy of 13 TeV and $m_{\text{H}} = 125\,\text{GeV}$, and subdominantly through vector boson fusion (VBF), with a smaller production cross section $\sigma_{\text{VBF}} = 1.726^{+0.03\%}_{-0.04\%} \pm 2.1\%(\text{PDF} + \alpha_{\text{S}})$ fb [11]. At leading order, the ggF production mode has contributions from diagrams that involve the trilinear HHH Higgs self-coupling and the emission of two Higgs bosons through a top quark loop, while the VBF production mode has contributions from three diagrams involving the trilinear HHH, HVV, and quartic HHVV couplings (Fig. 1). It also features the distinct final state signature of two, typically forward, jets in addition to the two Higgs bosons.

The production cross section and kinematic properties of the HH system are altered if values of the Higgs self-coupling, the top Yukawa coupling, and/or the quartic HHVV coupling are modified due to beyond the SM (BSM) effects. Notably, at the energy scale of the LHC, the leading contribution to the VBF production amplitude is the scattering of longitudinal vector bosons, which scales as $\sim m_{\text{HH}}^2(\kappa_{2V} - \kappa_V^2)$ [12], where, using an effective field theory (EFT) approach, κ_λ, κ_{2V}, and κ_V are defined to be multiplicative modifiers of the HHH, HHVV, and HVV couplings from their SM values, respectively.

In the SM, with $\kappa_{2V} = \kappa_V = 1$, VBF production is suppressed since the left-most $(\text{HVV})^2$ and right-most HHVV VBF diagrams in Fig. 1 cancel; however, BSM deviations to HHVV can spoil the cancelation, significantly enhancing this mode. This departure from the SM could be more
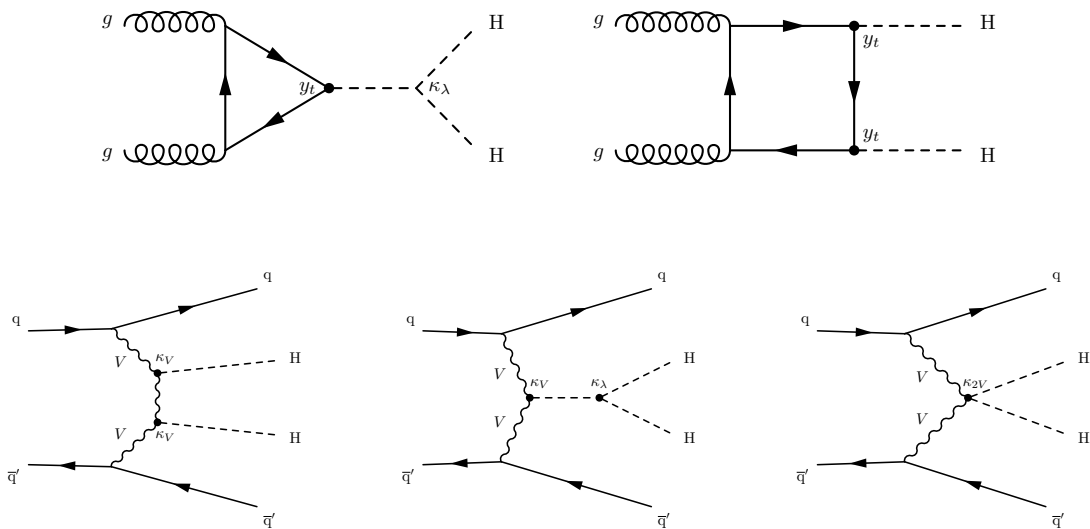

Figure 1: Leading-order diagrams for nonresonant Higgs boson pair production via gluon-gluon fusion (top) and vector boson fusion (bottom). In this note, we refer to the left-most VBF diagram as the $(\text{HVV})^2$ and the right-most as the HHVV diagram.
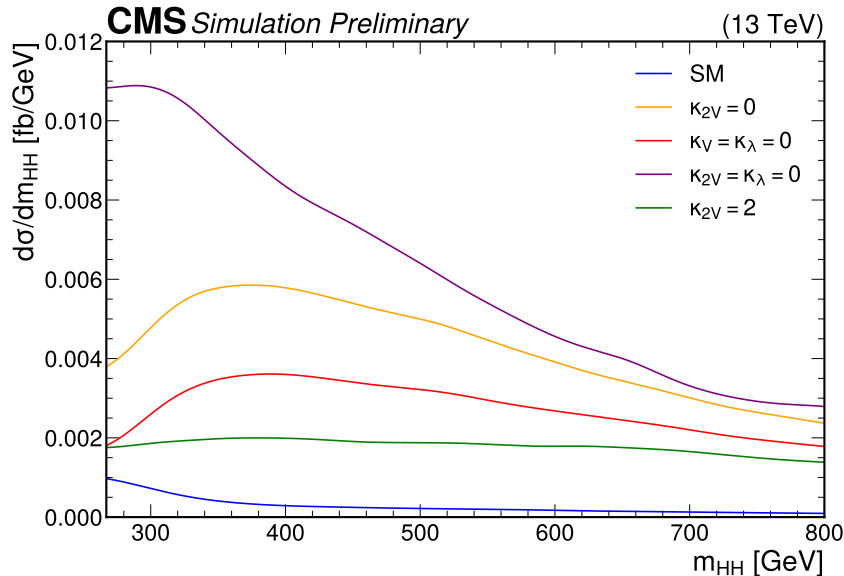
Figure 2: Differential cross section at 13 TeV center of mass for VBF HH production as a function of the invariant mass of the HH system (m_{HH}) for different diagrams and couplings.

visible at high energies. This is illustrated in Fig. 2, which shows the increase and shift towards higher m_{HH} of the differential VBF HH production cross section for enhanced and reduced $\kappa_{2\mathrm{V}}$ values. Thus, measuring high-m_{HH} nonresonant VBF HH production, with both Higgs bosons highly Lorentz-boosted, is a powerful probe of the HHVV coupling.

This is evidenced by the current $\kappa_{2\mathrm{V}}$ constraint in CMS being dominated by the search for boosted HH in the $b\bar{b}b\bar{b}$ channel, with an observed (expected) 95% confidence level (CL) constraint of $[0.6, 1.4]$ ($[0.7, 1.4]$), excluding $\kappa_{2\mathrm{V}} = 0$ for the first time [13]. This is followed by CMS searches in the resolved $b\bar{b}b\bar{b}$ [14] and $b\bar{b}\tau\tau$ [15] channels, with constraints of $[-0.1, 2.2]$ ($[-0.4, 2.5]$) and $[-0.4, 2.6]$ ($[-0.6, 2.8]$), respectively. Similarly, the strongest $\kappa_{2\mathrm{V}}$ constraint from the ATLAS experiment is from the boosted $b\bar{b}b\bar{b}$ search [16], with an observed (expected) 95% CL constraint of $[0.55, 1.49]$ ($[0.3, 1.7]$).

The success of searches in the boosted $b\bar{b}b\bar{b}$ channel motivates further exploration of high-m_{HH} HH production. This analysis presents the first search in the all-hadronic $b\bar{b}VV$ channel, where one Higgs boson decays to $b\bar{b}$ while the other to WW or ZZ, where $W \to qq$ and $Z \to qq$. The branching fractions for the $b\bar{b}$ and all-hadronic VV decays are 0.58 and 0.11 respectively, for a total branching fraction $\mathcal{B}(\mathrm{HH} \to b\bar{b}VV \to b\bar{b}4q) = 2 \cdot 0.58 \cdot 0.11 = 0.13$, which is the second largest behind $b\bar{b}b\bar{b}$. The analysis primarily aims to constrain $\kappa_{2\mathrm{V}}$ and also sets an exclusion limit on the inclusive HH production cross-section. It is not expected to be sensitive to κ_λ because of the focus on the high-m_{HH} regime.

Another benefit of the high-m_{HH} regime is the significantly reduced quantum chromodynamics (QCD) multijet background, which otherwise makes such all-hadronic searches extremely challenging. Because of the two Higgs bosons' high Lorentz-boosts, this regime also features the unique experimental signature of the $b\bar{b}$ and $VV \to 4q$ decays each being reconstructed as single wide-radius jets. Such merged $H \to b\bar{b}$ jets have been identified to great effect in CMS using deep neural networks (DNNs) [13, 17], but attaining similar signal versus background discrimination for $H \to VV$ jets remains an open challenge. To this end, we introduce a new attention-based DNN, referred to as the global particle transformer (GloParT) to not only enable this search but open new possibilities for searches in boosted-VV channels as well.

2 CMS Detector

The central feature of the CMS apparatus is a superconducting solenoid of 6 m internal diameter, providing a magnetic field of 3.8 T. Within the solenoid volume are a silicon pixel and strip tracker, a lead tungstate crystal electromagnetic calorimeter (ECAL), and a brass and scintillator hadron calorimeter (HCAL), each composed of a barrel and two endcap sections. Forward calorimeters extend the pseudorapidity (η) coverage provided by the barrel and endcap detectors. Muons are measured in gas-ionization detectors embedded in the steel flux-return yoke outside the solenoid. A more detailed description of the CMS detector, together with a definition of the coordinate system used and the relevant kinematic variables, can be found in Ref. [18].

Events of interest are selected using a two-tiered trigger system. The first level (L1), composed of custom hardware processors, uses information from the calorimeters and muon detectors to select events at a rate of around 100 kHz within a fixed latency of 4 μs [19]. The second level, known as the high-level trigger (HLT), consists of a farm of processors running a version of the full event reconstruction software optimized for fast processing, and reduces the event rate to around 1 kHz before data storage [20].

A particle-flow algorithm [21] aims to reconstruct and identify each individual particle in an event, with an optimized combination of information from the various elements of the CMS detector. The energy of photons is obtained from the ECAL measurement. The energy of electrons is determined from a combination of the electron momentum at the primary interaction vertex as determined by the tracker, the energy of the corresponding ECAL cluster, and the energy sum of all bremsstrahlung photons spatially compatible with originating from the electron track. The energy of muons is obtained from the curvature of the corresponding track. The energy of charged hadrons is determined from a combination of their momentum measured in the tracker and the matching ECAL and HCAL energy deposits, corrected for the response function of the calorimeters to hadronic showers. Finally, the energy of neutral hadrons is obtained from the corresponding corrected ECAL and HCAL energies. The primary vertex (PV) is taken to be the vertex corresponding to the hardest scattering in the event, evaluated using tracking information alone, as described in Section 9.4.1 of Ref. [22].

For each event, hadronic jets are clustered from these reconstructed particles using the infrared and collinear safe anti-k_T algorithm [23, 24] with a distance parameter of 0.4 (AK4 jets) or 0.8 (AK8 jets). Jet momentum is determined as the vectorial sum of all particle momenta in the jet, and is found from simulation to be, on average, within 5 to 10% of the true momentum over the whole p_T spectrum and detector acceptance. Additional proton-proton interactions within the same or nearby bunch crossings (pileup) can contribute additional tracks and calorimetric energy depositions to the jet momentum. The charged-hadron subtraction [25] and pileup per particle identification [26, 27] algorithms are used to mitigate the effect of pileup on AK4 and AK8 jets, respectively, and further corrections are applied to their energy and mass scales and resolutions to correct for detector mismodeling.

Electrons falling within the tracker acceptance are reconstructed using momentum derived from the tracker, the energy from the corresponding ECAL cluster, and the collective energy of all bremsstrahlung photons spatially aligned with the electron track [28]. Muons falling within the muon chamber acceptance $|\eta| < 2.4$ are reconstructed as tracks in the central tracker which align with tracks or hits in the muon chambers [29]. Electron candidates are required to fall within the tracker acceptance of $|\eta| < 2.5$ and have $p_\mathrm{T} > 20$ GeV, while muon candidates are required to be within the muon chamber acceptance of $|\eta| < 2.4$ and have $p_\mathrm{T} > 10$ GeV. Both leptons are then required to pass additional identification criteria [28, 29] to improve purity

and be isolated [21] to suppress those originating from bottom or charm hadron decays.

3 Event Simulation

The HH production in the ggF channel is simulated at next-to-leading-order (NLO) accuracy in perturbative QCD using POWHEG 2.0 [30–33], while the VBF channel is simulated at leading-order (LO) accuracy using MADGRAPH5_aMC@NLO 2.6.5 [34]. A basis of samples is simulated in variations of the κ_{2V}, κ_λ, and κ_V couplings. For ggF, the basis corresponds to $\kappa_\lambda = 1$, $\kappa_\lambda = 2.45$, and $\kappa_\lambda = 5$, while for VBF, the basis is $(\kappa_V = 1, \kappa_{2V} = 1, \kappa_\lambda = 1)$, $(\kappa_V = 1, \kappa_{2V} = 1, \kappa_\lambda = 0)$, $(\kappa_V = 1, \kappa_{2V} = 1, \kappa_\lambda = 2)$, $(\kappa_V = 1, \kappa_{2V} = 0, \kappa_\lambda = 1)$, $(\kappa_V = 1, \kappa_{2V} = 2, \kappa_\lambda = 1)$, and $(\kappa_V = 1.5, \kappa_{2V} = 1, \kappa_\lambda = 1)$. Linear combinations of these samples are used to simulate all possible variations. The production cross sections of the ggF samples are normalized to the next-to-NLO (NNLO) predictions for each coupling value [9, 35–40], while the SM VBF production cross section is normalized to the next-to-NNLO (N³LO) predictions with the same N³LO/LO correction applied to all other couplings.

The primary background of QCD multijet events is estimated purely through data. Top quark events, such as single t- and $t\bar{t}$ pair-production in association with jets, are simulated at the NLO QCD precision with POWHEG 2.0 [30–32, 41, 42]. V+jets events are simulated at LO accuracy with MADGRAPH5_aMC@NLO. Jets from the matrix element calculations and parton shower description are matched using the MLM prescription [34]. Diboson events are also simulated at LO accuracy. SM ggF H events are simulated at NNLO with POWHEG 2.0 [33, 43]. The POWHEG generator is also used to model VBF H, VH, and $t\bar{t}$H processes at NLO [44–46].

The parton showering, hadronization, and underlying event interactions for all processes are simulated using PYTHIA 8.205 [47] and the CP5 [48] tune. The parton distribution functions used correspond to those from NNPDF 3.0 [49] and 3.1 [50]. The response of the CMS detector is modeled with the GEANT4 package, with pileup emulated via mixing of simulated minimum-bias interactions.

4 Event Reconstruction and Selection

The primary physics objects considered in this analysis are large-radius (AK8) jets representing the two Higgs bosons. AK4 jets are also used in the online selection and to identify VBF HH production. As we do not expect any isolated leptons in our signal, events containing any isolated electrons and muons are vetoed.

The online selection is based on the combination of several conditions. Events with a scalar sum of jet transverse momenta H_T of at least 800, 900, or 1050 GeV, depending on the data-taking period, are selected. Events containing at least one AK8 jet with p_T of at least 400 or 500 GeV, where in the former case, the jet is required to have a trimmed mass of at least 40 GeV, are also chosen. Finally, triggers requiring an H_T of 750 and 800 GeV with all jets possessing "trimmed masses" of at least 50 GeV are considered as well, where the trimmed mass is defined as the invariant mass of the jet constituents after a jet trimming procedure [51] to remove soft and wide-angle radiation, using a subjet size parameter of 0.3 and a subjet-to-AK8 jet p_T fraction of 0.1. The trigger selection efficiency varies between 10 and 95% for jets with $300 < p_T < 450$ GeV and is fully efficient for jets with $p_T > 500$ GeV.

Both the H $\rightarrow$ b$\bar{b}$ and H $\rightarrow$ VV decays are then targeted through an offline selection for two highly boosted AK8 jets with a minimum p_T of 300 GeV and $|\eta| < 2.4$. The ParticleNet graph neural network (GNN) algorithm [52] is used to isolate the signal H $\rightarrow$ b$\bar{b}$ jets against

Table 1: Offline selection criteria for the signal and fail analysis regions.

VBF Region	ggF Region	Fail Region
No electrons or muons ≥ 2 AK8 jets $p_T > 300\,\text{GeV}$ (all jets) $\lvert\eta\rvert < 2.4$ (all jets) $50 < m_{\text{reg}} < 250\,\text{GeV}$ (all jets) $T_{\text{Xbb}} > 0.8$ (at least one jet) Jet assignment: $H \rightarrow b\bar{b}$: highest T_{Xbb} score $H \rightarrow VV$: out of remaining jets, highest GloParT score		
$T_{\text{Xbb}}^{\text{bb}} \geq$ VBF T_{Xbb} WP $\text{BDT}_{\text{VBF}} \geq$ VBF BDT WP	Not passing VBF selections $T_{\text{Xbb}}^{\text{bb}} \geq$ ggF T_{Xbb} WP $\text{BDT}_{\text{ggF}} \geq$ ggF BDT WP	$T_{\text{Xbb}}^{\text{bb}} <$ ggF T_{Xbb} WP
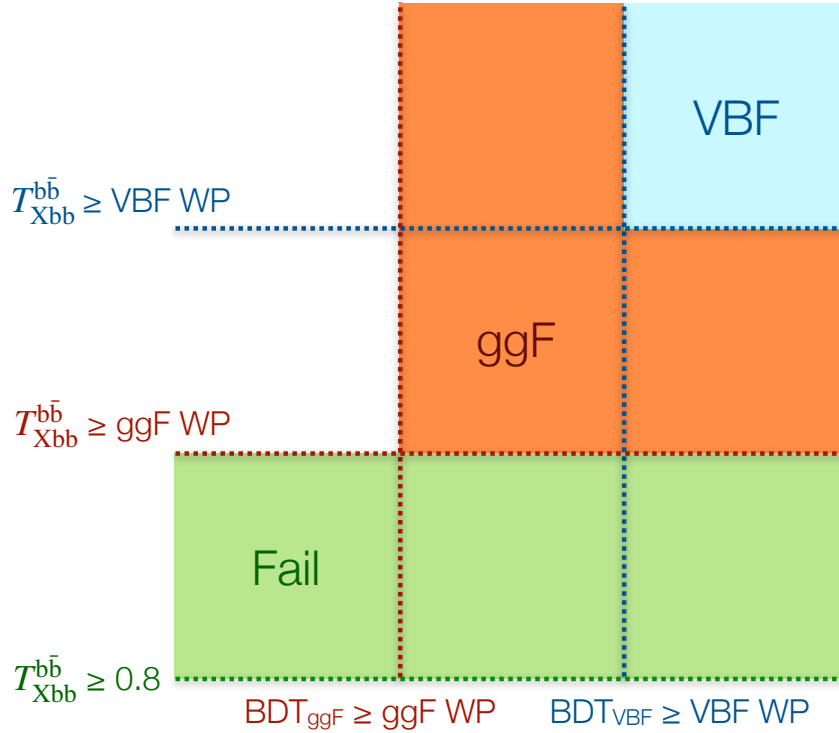
Figure 3: Illustration of the signal and fail analysis region selections in terms of the $T_{\text{Xbb}}^{\text{b}\bar{\text{b}}}$ and BDT scores.

background QCD jets using a discriminant, T_{Xbb}, derived from its outputs, while to identify the $H \rightarrow VV \rightarrow 4q$ jets, we introduce the new GloParT DNN, based on the ParticleTransformer (ParT) architecture [53], described in Section 5. Both networks have been decorrelated from the mass of the jets by enforcing a uniform distribution in jet mass and p_T in the training samples [17], to aid with their calibration. Additionally, as the jet mass resolution is crucial to the sensitivity of the search, we optimize the mass reconstruction for all AK8 jets us-

ing a ParticleNet-based regression algorithm trained to learn the true event-generator-level jet mass [54], the output of which we refer to as the regressed jet mass, or m_{reg}. The jet with the higher (lower) T_{Xbb} score is considered the $b\bar{b}$- (VV-) candidate jet.

The VBF process produces two, likely forward, jets with large invariant masses and pseudorapidity separations. To identify this mode, we select up to two AK4 jets per event, required to have $p_T > 25\,\text{GeV}$, $|\eta| < 4.7$, and a ΔR separation of 1.2 and 0.8, respectively, from the $b\bar{b}$- and VV-candidate AK8 jets. Out of the selected events, the two highest p_T jets are considered the VBF-jet candidates, and their invariant mass and pseudorapidity separation are used as input variables in a boosted decision tree (BDT) to discriminate against QCD and other backgrounds. These VBF-jet features are zero-padded for events with fewer than two jets passing the VBF-jet selections. Other input variables include outputs from the GloParT tagger and the two selected AK8 jets' kinematics. The variables are optimized to provide the highest BDT performance while remaining decorrelated from the mass of the $b\bar{b}$-candidate jet.

The BDT is optimized simultaneously for both the SM ggF and BSM VBF $\kappa_{2V} = 0$ signals, and separate "ggF" and "VBF" signal regions are defined using the BDT probabilities for the respective processes, referred to as BDT_{ggF} and BDT_{VBF}. Separate BDTs for the two processes were also tested, and the difference in performance was negligible. Concretely, the VBF region is defined by selections on the T_{Xbb} score of the $b\bar{b}$-candidate jet (T_{Xbb}^{bb}) and the BDT_{VBF} discriminant, corresponding to VBF signal (background) efficiencies of 40% ($\approx 0.1\%$) and 20% ($\approx 0.003\%$), respectively, chosen to optimize the expected exclusion limit on the VBF signal. The ggF region is defined by a veto on events passing the VBF selections along with selections on the T_{Xbb}^{bb} and BDT_{ggF} discriminants, corresponding to ggF signal (background) efficiencies of 60% ($\approx 0.3\%$) and 7% ($\approx 0.01\%$), respectively, similarly chosen to optimize the limit on the ggF signal. These selections are referred to as the ggF and VBF T_{Xbb}^{bb} and BDT working points (WPs).

To avoid biasing the analysis, these selections are optimized using a data-driven estimate for QCD multijet background performed only in the sidebands around m_H. The T_{Xbb} discriminant's signal efficiencies are calibrated using boosted gluon splitting to bottom quark ($g \to b\bar{b}$) jets in data and simulations [17], with p_T-dependent scale factors and uncertainties applied to the HH signals. The uncertainty on the BDT signal efficiency is dominated by that of the GloParT tagger and is calibrated based on a new technique using the ratio of the primary Lund jet plane [55] densities of each individual quark-subjet, described below in Section 5.1.

The search is performed by constructing a likelihood in the pass region as a function of the regressed mass of the $b\bar{b}$ candidate jet (m_{reg}^{bb}). The QCD multijet background contribution in the pass region is estimated through data in a "fail" region, defined using the same baseline selections on the two AK8 jets, but with the T_{Xbb} selection inverted, as described in Section 6 below. A summary of all offline selections is provided in Table 1, and the signal and fail region selections in terms of the T_{Xbb}^{bb} and BDT scores are illustrated in Fig. 3.

5 H $\to$ VV jet identification with GloParT

Effectively discriminating merged H $\to$ b$\bar{b}$ and H $\to$ VV jets from QCD jets is critical to the sensitivity of this search. The ParticleNet classifier is used for tagging H $\to$ b$\bar{b}$ jets, as in the CMS boosted HH $\to$ b$\bar{b}$b$\bar{b}$ search [13]. For identifying H $\to$ VV jets, we introduce a new transformer-based model, based on the ParT architecture, called the global particle transformer (GloParT).

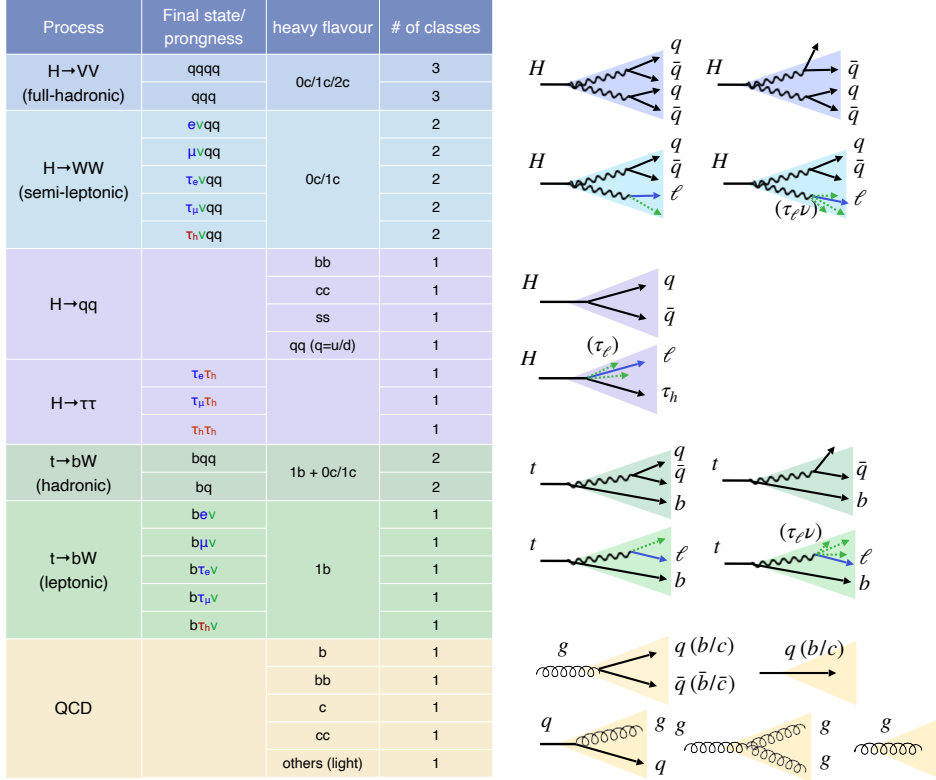| Process	Final state/ prongness	heavy flavour	# of classes
H→VV (full-hadronic)	qqqq	0c/1c/2c	3
	qqq		3
H→WW (semi-leptonic)	eνqq	0c/1c	2
	μνqq		2
	τ_eνqq		2
	τ_μνqq		2
	τ_hνqq		2
H→qq		bb	1
		cc	1
		ss	1
		qq (q=u/d)	1
H→ττ	τ_eτ_h		1
	τ_μτ_h		1
	τ_hτ_h		1
t→bW (hadronic)	bqq	1b + 0c/1c	2
	bq		2
t→bW (leptonic)	beν	1b	1
	bμν		1
	bτ_eν		1
	bτ_μν		1
	bτ_hν		1
QCD		b	1
		bb	1
		c	1
		cc	1
		others (light)	1

Figure 4: Full set of training jet classes for GloParT.

GloParT is trained to classify between background QCD jets and a wide variety of fully hadronic and semi-leptonic Higgs and top quark processes. The full set of training classes is shown in Fig. 4. To achieve mass decorrelation, the masses of Higgs- and top-quark-like resonances are varied in the training samples. Specifically, Higgs-like topologies are simulated using spin-0 particles (G) decaying to HH and top-quark-like topologies with G decaying to $t\bar{t}$, where the H and t masses are varied between 15 and 250 GeV. This ensures the tagger is not able to learn information about the resonance masses, but rather only the jet substructure. Mass decorrelation with respect to the H → VV jet is not strictly necessary for this search as the signal is extracted only through the $b\bar{b}$-jet distribution; however, it allows the tagger to be more generally applicable. For H → VV decays, the W and Z boson masses are also varied, either linearly with the H mass, for SM Higgs boson searches such as this one, or independently, motivated by BSM scenarios.

The final states for each process are grouped by the number of quarks and leptons per jet, and then further separated by heavy flavors. Notably, fully hadronic H → VV jets are separated into 4- and 3-pronged jets (qqqq and qqq), to account for boosted jets which may not capture all four VV daughter quarks. The inputs to the model are AK8 jets with up to 128 PF candidates and 7 secondary vertices, with features listed in Table 2, and the outputs are the probabilities of the jet to have originated from each of the aforementioned processes and final states. Although the GloParT model is also trained on H → $b\bar{b}$ jets, it has not yet been calibrated for that final state; hence, we use ParticleNet for $b\bar{b}$-tagging.

To evaluate the performance of the tagger, we use a single discriminant focusing on differentiating between the hadronic H → VV final states and top quark and QCD multijet backgrounds,
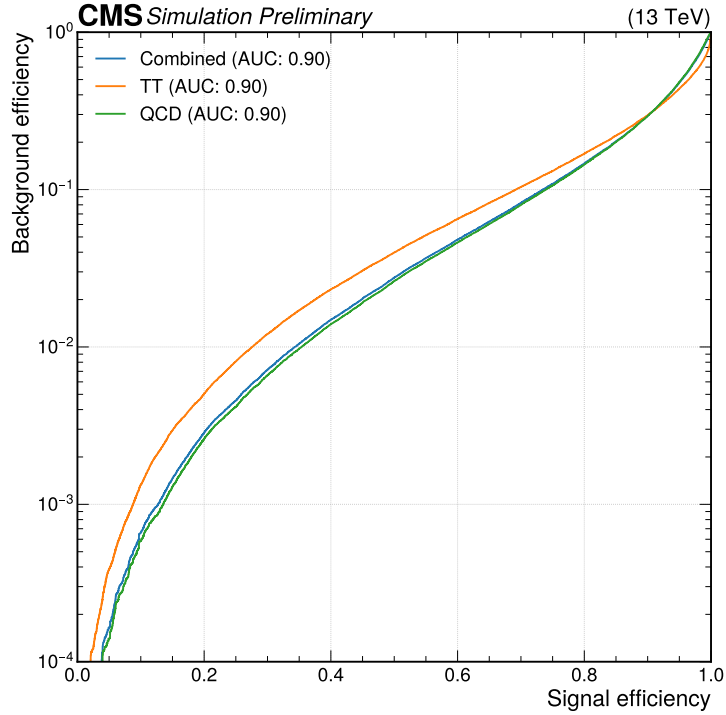
Figure 5: Receiver operating characteristic (ROC) curve for the T_{HVV} discriminator on VV-candidate jets passing the AK8 online and offline selections for SM HH signal versus QCD and $t\bar{t}$ backgrounds.

defined as

$$T_{\text{HVV}} = \frac{P_{\text{HVV4q}} + P_{\text{HVV3q}}}{P_{\text{QCD}} + P_{\text{Top}} + P_{\text{HVV4q}} + P_{\text{HVV3q}}}, \tag{1}$$

where P_{HVV4q}, P_{HVV3q}, P_{QCD}, and P_{Top} are the sum of the predicted probabilities of their respective sub-categories. The performance of this discriminant on VV-candidate jets passing our AK8 online and offline selections is shown in Fig. 5. In the analysis, the raw P_{HVV4q}, P_{HVV3q}, P_{QCD}, and P_{Top} are used as inputs to the BDT.

5.1 Calibration using the Lund jet plane

Unlike boosted $H \to b\bar{b}$ calibration, where we can use $g \to b\bar{b}$ jets as a proxy to measure data versus signal MC disagreement, it is difficult to define a control region dominated by an SM candle for the 4-pronged $H \to VV \to 4q$ jets. We instead use a method that measures data versus MC differences in the per-subjet radiation pattern based on densities of their primary Lund jet planes [55]. The primary Lund plane of a jet represents each successive hardest splitting in the 2D $(\ln(1/\Delta), \ln(k_T/\text{GeV}))$ plane, where Δ is the angular separation between the emitting and emitted particles and k_T is the product of Δ and the p_T of the emitted particle. As discussed in Ref. [55], the primary Lund plane captures key physics and substructure information about the jet. The ratio of the densities of primary Lund planes in data and simulation are measured in Ref. [56] per subjet in merged two-pronged jets originating from W bosons, clustered with the k_T algorithm [57, 58] to two exclusive jets, and binned in subjet p_T.

To measure a correction for the signal efficiency, first, a data-to-MC relative weight per event is derived for the signal by calculating the primary Lund plane splittings for each subjet in the $H \to VV$ jet and taking the product across the subjets of each splitting's data-to-MC correction factor as a function of its k_T, Δ, and subjet p_T. The ratio of the signal yield after following

Table 2: The complete set of input features into GloParT. Three types of inputs are considered: charged PF candidates, neutral PF candidates, and secondary vertices (SVs).

Variable	Definition
charged PF candidates	
$\log p_{\mathrm{T}}$	logarithm of the particle p_{T}
$\log E$	logarithm of the particle energy
$\Delta\eta(\mathrm{jet})$	difference in pseudorapidity between the particle and the jet axis
$\Delta\phi(\mathrm{jet})$	difference in azimuthal angle between the particle and the jet axis
$\lvert\eta\rvert$	absolute value of the particle pseudorapidity
q	electric charge of the particle
isMuon	true if the particle is identified as a muon
isElectron	true if the particle is identified as an electron
isChargedHadron	true if the particle is identified as a charged hadron
pvAssociationQuality	flag related to the association of the track to the primary vertices
lostInnerHits	quality flag of the track related to missing hits on the pixel layers
χ^2/dof	χ^2 value of the trajectory fit normalized to the number of degrees of freedom
qualityMask	quality flag of the track
d_z	longitudinal impact parameter of the track
d_z/σ_{d_z}	significance of the longitudinal impact parameter
d_{xy}	transverse impact parameter of the track
$d_{xy}/\sigma_{d_{xy}}$	significance of the transverse impact parameter
η_{rel}	pseudorapidity of the track relative to the jet axis
$p_{\mathrm{T,rel}}$ ratio	track momentum perpendicular to the jet axis, divided by the magnitude of the track momentum
$p_{\mathrm{par,rel}}$ ratio	track momentum parallel to the jet axis divided by the magnitude of the track momentum
$d_{3\mathrm{D}}$	signed 3D impact parameter of the track
$d_{3\mathrm{D}}/\sigma_{3\mathrm{D}}$	signed 3D impact parameter significance of the track
trackDistance	distance between the track and the jet axis at their point of closest approach
Neutral PF candidates	
$\log p_{\mathrm{T}}$	logarithm of the particles p_{T}
$\log E$	logarithm of the particles energy
$\Delta\eta(\mathrm{jet})$	difference in pseudorapidity between the particle and the jet axis
$\Delta\phi(\mathrm{jet})$	difference in azimuthal angle between the particle and the jet axis
$\lvert\eta\rvert$	absolute value of the particle pseudorapidity
isPhoton	true if the particle is identified as a photon
isNeutralHadron	true if the particle is identified as a neutral hadron
For SVs within the jet cone	
$\log p_{\mathrm{T}}$	logarithm of the SV p_{T}
m_{SV}	invariant mass of the tracks associated with the SV
$\Delta\eta(\mathrm{jet})$	difference in pseudorapidity between the SV and the jet axis
$\Delta\phi(\mathrm{jet})$	difference in azimuthal angle between the SV and the jet axis
$\lvert\eta\rvert$	absolute value of the SV pseudorapidity
N_{tracks}	number of tracks associated with the SV
χ^2/dof	χ^2 value of the SV fit normalized to the number of degrees of freedom
$d_{2\mathrm{D}}$	signed 2D impact parameter (i.e., in the transverse plane) of the SV
$d_{2\mathrm{D}}/\sigma_{2\mathrm{D}}$	signed 2D impact parameter significance of the SV
$d_{3\mathrm{D}}$	signed 3D impact parameter of the SV
$d_{3\mathrm{D}}/\sigma_{3\mathrm{D}}$	signed 3D impact parameter significance of the SV

the BDT selection with and without these event weights is then defined to be the data-to-MC correction, which is applied as a scale factor to each signal's overall yield, independently in the ggF and VBF regions. Uncertainties from the correction procedure are propagated as systematic uncertainties in the scale factor. These include statistical uncertainties on the derived Lund plane ratio, due to the limited number of data events in the W boson enriched sample,
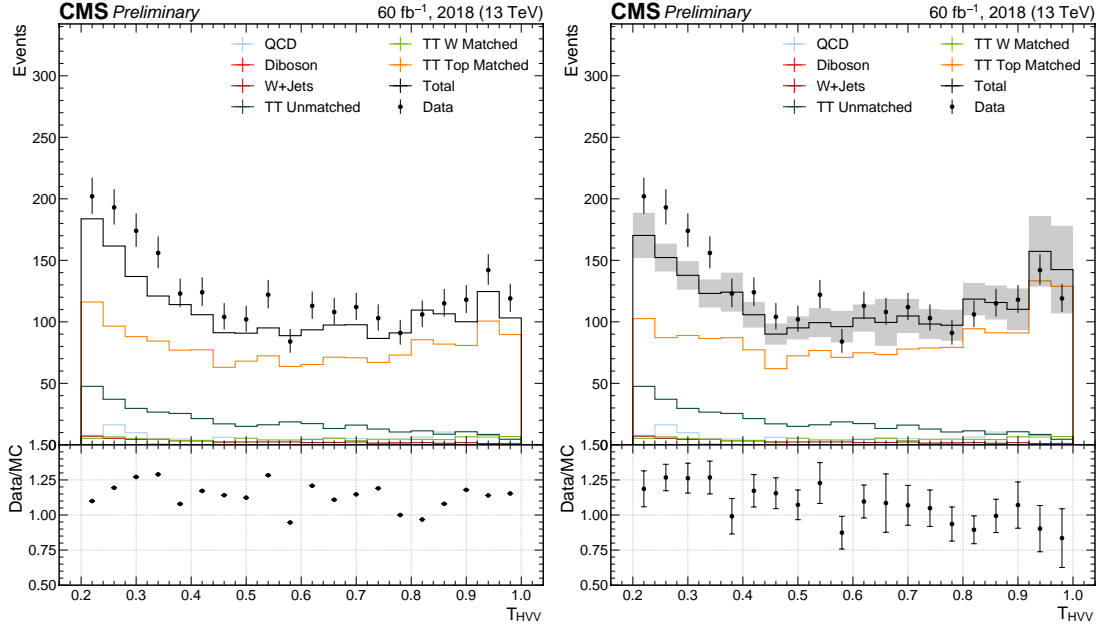
Figure 6: Distributions of the GloParT T_{HVV} discriminant before (left) and after (right) the Lund plane reweighting of top matched jets. The combined uncertainties from Lund-plane-based scale factors on the MC yield per bin are shown in gray, and are propagated to the data/MC ratio intervals.

and systematic uncertainties on the ratio, stemming from the MC modeling. Additionally, an uncertainty accouting for the extrapolation to high p_T subjets and an uncertainty accounting for the assumption of quark-subjet matching are included, as described in detail in Ref. [56]. A summary of the measured scale factors and uncertainties for different HH signals and signal regions is provided in Table 3. We note that while, in principle, this method could be used to calibrate the background efficiencies as well, this is not deemed necessary as the dominant background of QCD multijet events is estimated purely from data and the modeling of the subdominant backgrounds considers several other large sources of systematic uncertainties, as described in Section 7.

Table 3: Signal efficiency scale factors (SFs) and uncertainties for the BDT selection using the Lund jet plane for different HH signals and analysis regions. Both the total combined uncertainty and the components mentioned in the text are shown.

Signal Region	Process	SF ± unc.	Uncertainty components			
			Ratio MC modeling	Ratio statistical	Ratio p_T extrapolation	Subjet matching
ggF	SM ggF HH	1.05 ± 0.24	0.16	0.05	0.00	0.16
	SM VBF HH	1.17 ± 0.45	0.35	0.05	0.00	0.16
	VBF HH ($\kappa_{2V} = 0$)	1.09 ± 0.18	0.02	0.04	0.01	0.15
	VBF HH ($\kappa_{2V} = 2$)	1.10 ± 0.18	0.02	0.05	0.01	0.15
VBF	SM ggF HH	0.95 ± 0.28	0.26	0.08	0.01	0.12
	SM VBF HH	1.08 ± 0.46	0.38	0.05	0.01	0.19
	VBF HH ($\kappa_{2V} = 0$)	0.93 ± 0.27	0.16	0.06	0.02	0.23
	VBF HH ($\kappa_{2V} = 2$)	0.94 ± 0.27	0.16	0.05	0.02	0.23

The scale factor measurement is validated for GloParT on boosted top quark jets. We define a semi-leptonic boosted $t\bar{t}$ control region, tagging a leptonically-decaying top quark (t $\rightarrow$ bW $\rightarrow$ b$\mu\nu$), and then probing an opposite-side high p_T AK8 jet representing the hadronically-decaying quark. The event selection follows that of the control region in Ref. [56], comprising

online muon triggers and offline selections for a b-tagged AK4 jet, a leptonically-decaying W boson—based on the presence of a muon and missing transverse energy—and a high p_T AK8 jet with mass close to that of the top quark. Jets from the $t\bar{t}$ MC samples are categorized using generator-level particles as either: "top matched"—with all three daughter quarks lying within the jet; "W matched"—only the W daughter quarks inside the jet; or "unmatched"—neither of these two cases. Only the top-matched jets are reweighted with the Lund plane ratios.

We consider the T_{HVV} discriminant from Eq. (1), excluding P_{Top} in the denominator to retain top quark events in the high tagger score bins. Plots of the T_{HVV} distribution from the 2018 datasets before and after Lund-plane-reweighting of the top-matched-jet events are shown in Fig. 6. The combined uncertainties per bin are also shown in the distributions and data/MC ratios. We observe an overall improvement in data/MC agreement in the high T_{HVV} bins ($T_{\mathrm{HVV}} > 0.6$), with the χ^2-test value improving from 16.6 to 10.9. Importantly, the data and MC yields are all consistent within $1\,\sigma$ in these bins.

6 Background Estimation

The search is performed in the signal regions using a one-dimensional likelihood model binned in $m_{\mathrm{reg}}^{\mathrm{bb}}$. The background in these regions is dominated by QCD multijet events, and is estimated using the product of data in the fail region with polynomial transfer factors, as in several previous CMS boosted Higgs boson searches including HH $\rightarrow$ b$\bar{\mathrm{b}}$b$\bar{\mathrm{b}}$ [13, 59, 60], and as described below. Other minor backgrounds include top quark and vector boson backgrounds, which are estimated using MC simulation, systematic and statistical uncertainties for which are incorporated in the final statistical analysis. Deviations to the quartic coupling can also enhance VHH production. However, this process is suppressed in the VBF region because of the lepton veto, the selections for two forward jets, and its 10–100 times smaller production cross section for $\kappa_{2\mathrm{V}}$ deviations.

To estimate the QCD multijet background, its yield in each $m_{\mathrm{reg}}^{\mathrm{bb}}$ bin in the fail region is represented by an unconstrained parameter in the likelihood, whose initial value is set by the difference between the data and the total standard model MC background in that bin. The QCD yield in the corresponding bin of the signal regions is then determined by the product of the yield in the fail region with separate 1D "fail-to-pass" transfer functions, $T_{\mathrm{P/F}}^{R}(m_{\mathrm{reg}}^{\mathrm{bb}})$, for each region $R \in \{\mathrm{ggF}, \mathrm{VBF}\}$, evaluated at that bin in $m_{\mathrm{reg}}^{\mathrm{bb}}$. As both the H $\rightarrow$ b$\bar{\mathrm{b}}$ tagger and BDT are decorrelated with the jet mass, it is assumed that the shape of data in the fail and pass regions are largely similar, with any residual differences then corrected by $T_{\mathrm{P/F}}^{R}(m_{\mathrm{reg}}^{\mathrm{bb}})$.

Each transfer function is chosen to be a polynomial whose order is determined by independent Fisher F-tests [61] for the two signal regions, yielding a 0th-order (i.e. constant) $T_{\mathrm{P/F}}^{R}(m_{\mathrm{reg}}^{\mathrm{bb}}) = 4.9 \cdot 10^{-5}$ for the ggF region and a 1st-order $T_{\mathrm{P/F}}^{R}(m_{\mathrm{reg}}^{\mathrm{bb}}) = (0.3\,m_{\mathrm{reg}}^{\mathrm{bb}} - 3.2) \cdot 10^{-7}$ for the VBF region. The coefficients of the transfer function are fit simultaneously to the data in all three analysis regions, along with the signal and background systematic uncertainties and the HH signal strengths. The background estimate is validated for the two signal regions using goodness-of-fit tests based on the saturated model test statistic, which yield p-values of 0.09 and 0.47, respectively, indicating no significant disagreement between the data and our model. Studies are also performed using pseudodata to confirm that the background estimate does not bias the measured HH signal strengths.

7 Systematic Uncertainties

We consider several sources of theoretical and experimental systematic uncertainties on the signal and background modelling in the signal regions, which are summarized in Table 4. Overall, the dominant source of uncertainty on the HH signal strength is the statistical uncertainty in the QCD multijet background estimation, driven by the limited signal region sample size. This uncertainty has an impact on the best-fit signal strength of 50% relative to the overall uncertainty.

The uncertainties on the signal efficiency of $H \to b\overline{b}$ and $H \to VV$ are also significant. The $H \to b\overline{b}$ efficiency scale factors and uncertainties are measured for data versus simulation in a control region dominated by $g \to b\overline{b}$ jets [17] and represent a 10% relative impact. The $H \to VV$ efficiency scale factor and uncertainty measurements are described in Section 5.1 and vary depending on the production mode and different coupling strengths of the HH signal, representing an overall 23% relative impact.

Other significant sources of experimental uncertainty include the scale and resolution of the regressed jet mass and reconstructed jet energy [62] in data versus simulations. Jet mass corrections and uncertainties are measured in a control region enriched in $t\overline{t}$ events, using AK8 jets originating from hadronic W boson decays [63], and with a 7% impact, while jet energy corrections and uncertainties constitute 2%. Finally, there are large statistical uncertainties related to the MC simulations of the subdominant top quark and vector boson backgrounds, reaching 30% in some bins of the signal regions; these have an 8% impact.

On the theoretical side, there is a large uncertainty related to the HH production cross sections, which has a relative impact of up to 24% on best-fit signal strength. Uncertainties related to the parton showering performed using PYTHIA 8 [64] are propagated to the MC kinematic distributions and have a 15%, while QCD renormalization and factorization scale uncertainties are estimated by considering the envelope of distributions obtained by varying the scales by a factor of 2 and constitute a 5% impact.

Subdominant sources considered include uncertainties related to parton distribution functions (PDFs), H branching fractions, luminosity [65–67], pileup interactions, and trigger efficiencies, which have sub-percent-level impacts.

8 Results

A binned maximum likelihood fit is performed to the observed $m_{\mathrm{reg}}^{\mathrm{bb}}$ distributions simultaneously in the signal and fail regions, whose results are shown in Fig. 7. Upper limits on the HH production cross section and constraints on the κ_{2V} coupling at a 95% CL are derived based on the asymptotic formulae for the profile likelihood ratio test statistic [68, 69] and the $\mathrm{CL_s}$ [70, 71] criterion, and are shown in Figs. 8 and 9, respectively. To derive upper limits at different κ_{2V} values, the signal shapes are interpolated using a linear combination of simulations with varying couplings. The upper limit on the SM HH production cross section is observed (expected) to be 142 (69) and on the $\kappa_{2V} = 0$ benchmark 1.1 (0.9), relative to their theoretical predictions. Finally, the coupling modifier κ_{2V} is observed (expected) to be constrained within $[-0.04, 2.05]$ ($[0.05, 1.98]$) at 95% CL. These results have been determined using the CMS statistical analysis tool COMBINE [72], which is based on the ROOFIT [73] and ROOSTATS [74] frameworks.

Table 4: Summary of the effect of different systematic uncertainties on the signal or background yields.

Source	Processes affected	Uncertainty (combined %)
ggF HH production cross section	ggF HH	+5%/−19%
VBF HH production cross section	VBF HH	2.1%
$H \to b\bar{b}$ branching fraction	HH	1.25%
$H \to VV$ branching fraction	HH	1.53%
$H \to b\bar{b}$ tagging signal efficiency	HH	7–10%
$H \to VV$ tagging signal efficiency	HH	16–38%
QCD multijet background uncertainty	QCD multijet	10%
Parton showering	All MC	1–9%
Jet energy scale and resolution	All MC	1–3%
Jet mass scale and resolution	All MC	1–4%
MC statistical uncertainty	All MC	1–30%
QCD renormalization and factorization scale	All MC	7–10%
PDF	All MC	1–4%
Luminosity	All MC	1%
Pileup	All MC	1%
Trigger efficiency	All MC	<1%

9 Summary

We describe a search for standard model (SM) nonresonant Higgs boson pair (HH) production in the two bottom quark ($b\bar{b}$) and two vector boson (VV) all-hadronic final states. We search for two highly boosted Higgs bosons producing fully merged jets; where all H daughter quarks are contained within a single large-radius jet. The established ParticleNet mass-decorrelated tagger is used to select for $H \to b\bar{b}$ jets and we introduce the new high-performing GloParT tagger for $H \to VV$ jets. The HH signal is extracted using the $H \to b\bar{b}$ jet regressed mass using control regions with tagger scores inverted to obtain a data-driven estimate of the shape and normalization of the QCD multijet background via a parametric transfer function. The results are interpreted in terms of a multiplicative modifier of the SM quartic coupling between two Higgs bosons and two vector bosons, which is observed (expected) to be constrained to $[-0.04, 2.05]$ ($[0.05, 1.98]$) at 95% confidence level.
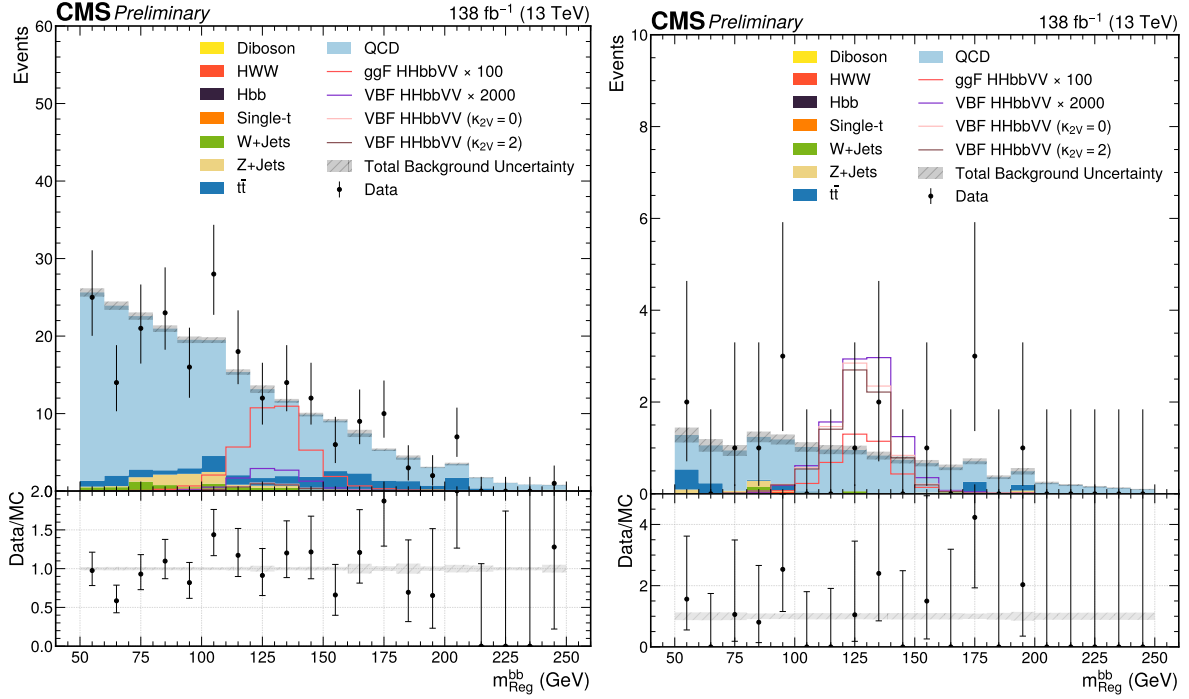
Figure 7: Post-background-only-fit distributions of the b$\bar{\text{b}}$-candidate jet regressed mass ($m_{\text{reg}}^{\text{bb}}$) in the ggF (left) and VBF (right) signal regions.
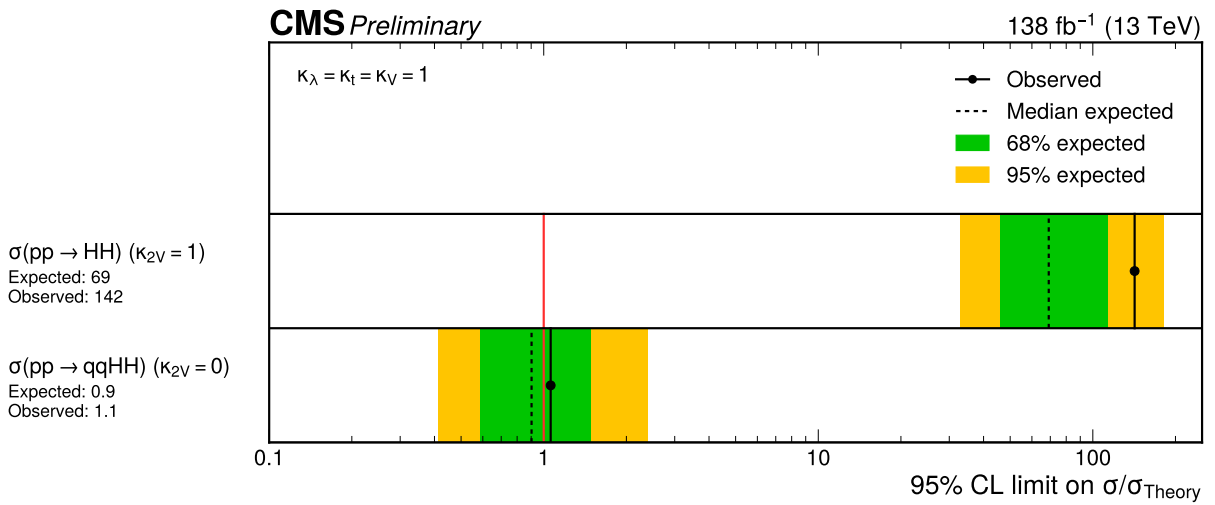

Figure 8: Observed and expected exclusion limits at 95% CL for the HH $\rightarrow$ b$\bar{\text{b}}$VV signal SM production cross section (top) and cross section at $\kappa_{2\text{V}} = 0$ (bottom).
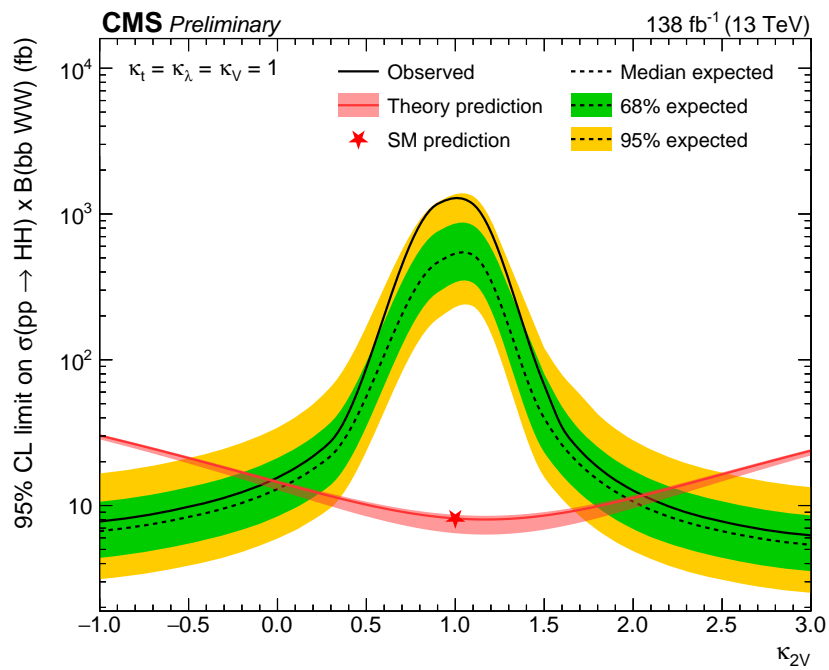
Figure 9: 1D upper limits scans on the inclusive HH production cross section as a function of κ_{2V} for $\kappa_t = \kappa_\lambda = \kappa_V = 1$.

References

[1] ATLAS and CMS Collaborations, "Combined Measurement of the Higgs Boson Mass in pp Collisions at $\sqrt{s} = 7$ and 8 TeV with the ATLAS and CMS Experiments", *Phys. Rev. Lett.* **114** (2015) 191803, `doi:10.1103/PhysRevLett.114.191803`, `arXiv:1503.07589`.

[2] CMS Collaboration, "A measurement of the Higgs boson mass in the diphoton decay channel", *Phys. Lett. B* **805** (2020) 135425, `doi:10.1016/j.physletb.2020.135425`, `arXiv:2002.06398`.

[3] ATLAS Collaboration, "Measurement of the Higgs boson mass in the $H \to ZZ^* \to 4\ell$ decay channel using 139 fb^{-1} of $\sqrt{s} = 13$ TeV pp collisions recorded by the ATLAS detector at the LHC", *Phys. Lett. B* **843** (2023) 137880, `doi:10.1016/j.physletb.2023.137880`, `arXiv:2207.00320`.

[4] CMS Collaboration, "Measurement of the Higgs boson width and evidence of its off-shell contributions to ZZ production", *Nature Phys.* **18** (2022) 1329, `doi:10.1038/s41567-022-01682-0`, `arXiv:2202.06923`.

[5] ATLAS Collaboration, "Evidence of off-shell Higgs boson production from ZZ leptonic decay channels and constraints on its total width with the ATLAS detector", *Phys. Lett. B* **846** (2023) 138223, `doi:10.1016/j.physletb.2023.138223`, `arXiv:2304.01532`.

[6] CMS Collaboration, "Combined measurements of Higgs boson couplings in proton–proton collisions at $\sqrt{s} = 13$ TeV", *Eur. Phys. J. C* **79** (2019) 421, `doi:10.1140/epjc/s10052-019-6909-y`, `arXiv:1809.10733`.

[7] CMS Collaboration, "A portrait of the Higgs boson by the CMS experiment ten years after the discovery", *Nature* **607** (2022) 60, `doi:10.1038/s41586-022-04892-x`, `arXiv:2207.00043`.

[8] ATLAS Collaboration, "A detailed map of Higgs boson interactions by the ATLAS experiment ten years after the discovery", *Nature* **607** (2022) 52, `doi:10.1038/s41586-022-04893-w`, `arXiv:2207.00092`. [Erratum: `doi:10.1038/s41586-022-05581-5`].

[9] M. Grazzini et al., "Higgs boson pair production at NNLO with top quark mass effects", *JHEP* **05** (2018) 059, `doi:10.1007/JHEP05(2018)059`, `arXiv:1803.02463`.

[10] J. Baglio et al., "$gg \to HH$: Combined uncertainties", *Phys. Rev. D* **103** (2021) 056002, `doi:10.1103/PhysRevD.103.056002`, `arXiv:2008.11626`.

[11] LHC Higgs Cross Section Working Group, "Handbook of LHC Higgs Cross Sections: 4. Deciphering the nature of the Higgs sector", *CERN Yellow Rep. Monogr.* **2** (2017) `doi:10.23731/CYRM-2017-002`, `arXiv:1610.07922`.

[12] F. Bishara, R. Contino, and J. Rojo, "Higgs pair production in vector-boson fusion at the LHC and beyond", *Eur. Phys. J. C* **77** (2017) 481, `doi:10.1140/epjc/s10052-017-5037-9`, `arXiv:1611.03860`.

[13] CMS Collaboration, "Search for nonresonant pair production of highly energetic Higgs bosons decaying to bottom quarks", *Phys. Rev. Lett.* **131** (2023) 041803, `doi:10.1103/PhysRevLett.131.041803`, `arXiv:2205.06667`.

[14] CMS Collaboration, "Search for Higgs Boson Pair Production in the four b quark final state in proton-proton collisions at $\sqrt{s}$=13 TeV", *Phys. Rev. Lett.* **129** (2022) 081802, `doi:10.1103/PhysRevLett.129.081802`, `arXiv:2202.09617`.

[15] CMS Collaboration, "Search for nonresonant Higgs boson pair production in final state with two bottom quarks and two tau leptons in proton-proton collisions at s=13 TeV", *Phys. Lett. B* **842** (2023) 137531, `doi:10.1016/j.physletb.2022.137531`, `arXiv:2206.09401`.

[16] ATLAS Collaboration, "Search for pair production of boosted Higgs bosons via vector-boson fusion in the $b\bar{b}b\bar{b}$ final state using pp collisions at $\sqrt{s} = 13$ TeV with the ATLAS detector", 2024. `arXiv:2404.17193`. Submitted to *Phys. Lett. B.*

[17] CMS Collaboration, "Performance of heavy-flavour jet identification in boosted topologies in proton-proton collisions at $\sqrt{s} = 13$ TeV", CMS Physics Analysis Summary CMS-PAS-BTV-22-001, 2023.

[18] CMS Collaboration, "The CMS experiment at the CERN LHC", *JINST* **3** (2008) S08004, `doi:10.1088/1748-0221/3/08/S08004`.

[19] CMS Collaboration, "Performance of the CMS Level-1 trigger in proton-proton collisions at $\sqrt{s} = 13$ TeV", *JINST* **15** (2020) P10017, `doi:10.1088/1748-0221/15/10/P10017`, `arXiv:2006.10165`.

[20] CMS Collaboration, "The CMS trigger system", *JINST* **12** (2017) P01020, `doi:10.1088/1748-0221/12/01/P01020`, `arXiv:1609.02366`.

[21] CMS Collaboration, "Particle-flow reconstruction and global event description with the CMS detector", *JINST* **12** (2017) P10003, `doi:10.1088/1748-0221/12/10/P10003`, `arXiv:1706.04965`.

[22] CMS Collaboration, "Technical proposal for the Phase-II upgrade of the Compact Muon Solenoid", CMS Technical Proposal CERN-LHCC-2015-010, CMS-TDR-15-02, 2015.

[23] M. Cacciari, G. P. Salam, and G. Soyez, "The anti-k_T jet clustering algorithm", *JHEP* **04** (2008) 063, `doi:10.1088/1126-6708/2008/04/063`, `arXiv:0802.1189`.

[24] M. Cacciari, G. P. Salam, and G. Soyez, "FastJet user manual", *Eur. Phys. J. C* **72** (2012) 1896, `doi:10.1140/epjc/s10052-012-1896-2`, `arXiv:1111.6097`.

[25] CMS Collaboration, "Pileup Removal Algorithms", CMS Physics Analysis Summary CMS-PAS-JME-14-001, 2014.

[26] D. Bertolini, P. Harris, M. Low, and N. Tran, "Pileup Per Particle Identification", *JHEP* **10** (2014) 059, `doi:10.1007/JHEP10(2014)059`, `arXiv:1407.6013`.

[27] CMS Collaboration, "Pileup mitigation at CMS in 13 TeV data", *JINST* **15** (2020) P09018, `doi:10.1088/1748-0221/15/09/p09018`, `arXiv:2003.00503`.

[28] CMS Collaboration, "Performance of Electron Reconstruction and Selection with the CMS Detector in Proton-Proton Collisions at $\sqrt{s} = 8$ TeV", *JINST* **10** (2015) P06005, `doi:10.1088/1748-0221/10/06/P06005`, `arXiv:1502.02701`.

[29] CMS Collaboration, "Performance of the CMS muon detector and muon reconstruction with proton-proton collisions at $\sqrt{s} = 13$ TeV", *JINST* **13** (2018) P06015, `doi:10.1088/1748-0221/13/06/P06015`, `arXiv:1804.04528`.

[30] P. Nason, "A new method for combining NLO QCD with shower Monte Carlo algorithms", *JHEP* **11** (2004) 040, `doi:10.1088/1126-6708/2004/11/040`, `arXiv:hep-ph/0409146`.

[31] S. Frixione, P. Nason, and C. Oleari, "Matching NLO QCD computations with parton shower simulations: the POWHEG method", *JHEP* **11** (2007) 070, `doi:10.1088/1126-6708/2007/11/070`, `arXiv:0709.2092`.

[32] S. Alioli, P. Nason, C. Oleari, and E. Re, "A general framework for implementing NLO calculations in shower Monte Carlo programs: the POWHEG BOX", *JHEP* **06** (2010) 043, `doi:10.1007/JHEP06(2010)043`, `arXiv:1002.2581`.

[33] E. Bagnaschi, G. Degrassi, P. Slavich, and A. Vicini, "Higgs production via gluon fusion in the POWHEG approach in the SM and in the MSSM", *JHEP* **02** (2012) 088, `doi:10.1007/JHEP02(2012)088`, `arXiv:1111.2854`.

[34] J. Alwall et al., "The automated computation of tree-level and next-to-leading order differential cross sections, and their matching to parton shower simulations", *JHEP* **07** (2014) 079, `doi:10.1007/JHEP07(2014)079`, `arXiv:1405.0301`.

[35] S. Dawson, S. Dittmaier, and M. Spira, "Neutral Higgs boson pair production at hadron colliders: QCD corrections", *Phys. Rev. D* **58** (1998) 115012, `doi:10.1103/PhysRevD.58.115012`, `arXiv:hep-ph/9805244`.

[36] D. de Florian and J. Mazzitelli, "Higgs Boson Pair Production at Next-to-Next-to-Leading Order in QCD", *Phys. Rev. Lett.* **111** (2013) 201801, `doi:10.1103/PhysRevLett.111.201801`, `arXiv:1309.6594`.

[37] D. de Florian and J. Mazzitelli, "Higgs pair production at next-to-next-to-leading logarithmic accuracy at the LHC", *JHEP* **09** (2015) 053, `doi:10.1007/JHEP09(2015)053`, `arXiv:1505.07122`.

[38] J. Baglio et al., "Gluon fusion into Higgs pairs at NLO QCD and the top mass scheme", *Eur. Phys. J. C* **79** (2019) 459, `doi:10.1140/epjc/s10052-019-6973-3`, `arXiv:1811.05692`.

[39] S. Borowka et al., "Higgs Boson Pair Production in Gluon Fusion at Next-to-Leading Order with Full Top-Quark Mass Dependence", *Phys. Rev. Lett.* **117** (2016) 012001, `doi:10.1103/PhysRevLett.117.079901`, `arXiv:1604.06447`. [Erratum: `doi:10.1103/PhysRevLett.117.079901`].

[40] D. Y. Shao, C. S. Li, H. T. Li, and J. Wang, "Threshold resummation effects in Higgs boson pair production at the LHC", *JHEP* **07** (2013) 169, `doi:10.1007/JHEP07(2013)169`, `arXiv:1301.1245`.

[41] T. Ježo et al., "An NLO+PS generator for $t\bar{t}$ and Wt production and decay including non-resonant and interference effects", *Eur. Phys. J. C* **76** (2016) 691, `doi:10.1140/epjc/s10052-016-4538-2`, `arXiv:1607.04538`.

[42] S. Frixione, P. Nason, and G. Ridolfi, "A Positive-weight next-to-leading-order Monte Carlo for heavy flavour hadroproduction", *JHEP* **09** (2007) 126, `doi:10.1088/1126-6708/2007/09/126`, `arXiv:0707.3088`.

[43] K. Hamilton, P. Nason, C. Oleari, and G. Zanderighi, "Merging H/W/Z + 0 and 1 jet at NLO with no merging scale: a path to parton shower + NNLO matching", *JHEP* **05** (2013) 082, `doi:10.1007/JHEP05(2013)082`, `arXiv:1212.4504`.

[44] P. Nason and C. Oleari, "NLO Higgs boson production via vector-boson fusion matched with shower in POWHEG", *JHEP* **02** (2010) 037, `doi:10.1007/JHEP02(2010)037`, `arXiv:0911.5299`.

[45] G. Luisoni, P. Nason, C. Oleari, and F. Tramontano, "HW$^\pm$/HZ+0 and 1 jet at NLO with the POWHEG box interfaced to GoSam and their merging within MiNLO", *JHEP* **10** (2013) 083, `doi:10.1007/JHEP10(2013)083`, `arXiv:1306.2542`.

[46] H. B. Hartanto, B. Jäger, L. Reina, and D. Wackeroth, "Higgs boson production in association with top quarks in the POWHEG BOX", *Phys. Rev. D* **91** (2015) 094003, `doi:10.1103/PhysRevD.91.094003`, `arXiv:1501.04498`.

[47] T. Sjöstrand et al., "An introduction to PYTHIA 8.2", *Comput. Phys. Commun.* **191** (2015) 159, `doi:10.1016/j.cpc.2015.01.024`, `arXiv:1410.3012`.

[48] CMS Collaboration, "Extraction and validation of a new set of CMS PYTHIA8 tunes from underlying-event measurements", *Eur. Phys. J. C* **80** (2020) 4, `doi:10.1140/epjc/s10052-019-7499-4`, `arXiv:1903.12179`.

[49] NNPDF Collaboration, "Parton distributions for the LHC Run II", *JHEP* **04** (2015) 040, `doi:10.1007/JHEP04(2015)040`, `arXiv:1410.8849`.

[50] NNPDF Collaboration, "Parton distributions from high-precision collider data", *Eur. Phys. J. C* **77** (2017) 663, `doi:10.1140/epjc/s10052-017-5199-5`, `arXiv:1706.00428`.

[51] D. Krohn, J. Thaler, and L.-T. Wang, "Jet Trimming", *JHEP* **02** (2010) 084, `doi:10.1007/JHEP02(2010)084`, `arXiv:0912.1342`.

[52] H. Qu and L. Gouskos, "ParticleNet: Jet Tagging via Particle Clouds", *Phys. Rev. D* **101** (2020) 056019, `doi:10.1103/PhysRevD.101.056019`, `arXiv:1902.08570`.

[53] H. Qu, C. Li, and S. Qian, "Particle Transformer for Jet Tagging", in *Proceedings of the 39th International Conference on Machine Learning*, K. Chaudhuri et al., eds., volume 162, p. 18281. 2022. `arXiv:2202.03772`.

[54] CMS Collaboration, "Mass regression of highly-boosted jets using graph neural networks", CMS Detector Performance Note CMS-DP-2021-017, 2021.

[55] F. A. Dreyer, G. P. Salam, and G. Soyez, "The Lund Jet Plane", *JHEP* **12** (2018) 064, `doi:10.1007/JHEP12(2018)064`, `arXiv:1807.04758`.

[56] CMS Collaboration, "Lund Plane Reweighting for Jet Substructure Correction", CMS Detector Performance Note CMS-DP-2023-046, 2023.

[57] S. Catani, Y. L. Dokshitzer, M. H. Seymour, and B. R. Webber, "Longitudinally invariant k_T clustering algorithms for hadron hadron collisions", *Nucl. Phys. B* **406** (1993) 187, `doi:10.1016/0550-3213(93)90166-M`.

[58] S. D. Ellis and D. E. Soper, "Successive combination jet algorithm for hadron collisions", *Phys. Rev. D* **48** (1993) 3160, `doi:10.1103/PhysRevD.48.3160`, `arXiv:hep-ph/9305266`.

[59] CMS Collaboration, "Search for a massive resonance decaying to a pair of Higgs bosons in the four b quark final state in proton-proton collisions at $\sqrt{s} = 13$ TeV", *Phys. Lett. B* **781** (2018) 244, `doi:10.1016/j.physletb.2018.03.084`, `arXiv:1710.04960`.

[60] CMS Collaboration, "Inclusive search for highly boosted Higgs bosons decaying to bottom quark-antiquark pairs in proton-proton collisions at $\sqrt{s} = 13$ TeV", *JHEP* **12** (2020) 85, `doi:10.1007/JHEP12(2020)085`, `arXiv:2006.13251`.

[61] R. A. Fisher, "On the interpretation of χ^2 from contingency tables, and the calculation of p", *J. Royal Statistical Society* **85** (1922) 87, `doi:10.2307/2340521`.

[62] CMS Collaboration, "Jet energy scale and resolution measurement with Run 2 Legacy Data Collected by CMS at 13 TeV", CMS Detector Performance Note CMS-DP-2021-033, 2021.

[63] CMS Collaboration, "Search for Higgs boson pair production via vector boson fusion with highly Lorentz-boosted Higgs bosons in the four b quark final state at $\sqrt{s} = 13$ TeV", CMS Physics Analysis Summary CMS-PAS-B2G-21-001, CERN, 2021.

[64] S. Mrenna and P. Skands, "Automated Parton-Shower Variations in Pythia 8", *Phys. Rev. D* **94** (2016) 074005, `doi:10.1103/PhysRevD.94.074005`, `arXiv:1605.08352`.

[65] CMS Collaboration, "Precision luminosity measurement in proton-proton collisions at $\sqrt{s} = 13$ TeV in 2015 and 2016 at CMS", *Eur. Phys. J. C* **81** (2021) 800, `doi:10.1140/epjc/s10052-021-09538-2`, `arXiv:2104.01927`.

[66] CMS Collaboration, "CMS luminosity measurement for the 2017 data-taking period at $\sqrt{s} = 13$ TeV", CMS Physics Analysis Summary CMS-PAS-LUM-17-004, 2018.

[67] CMS Collaboration, "CMS luminosity measurement for the 2018 data-taking period at $\sqrt{s} = 13$ TeV", CMS Physics Analysis Summary CMS-PAS-LUM-18-002, 2019.

[68] ATLAS and CMS Collaborations, and the LHC Higgs Combination Group, "Procedure for the LHC Higgs boson search combination in Summer 2011", ATL-PHYS-PUB-2011-011, CMS NOTE-2011/005, 2011.

[69] G. Cowan, K. Cranmer, E. Gross, and O. Vitells, "Asymptotic formulae for likelihood-based tests of new physics", *Eur. Phys. J. C* **71** (2011) 1554, `doi:10.1140/epjc/s10052-011-1554-0`, `arXiv:1007.1727`. [Erratum: `doi:10.1140/epjc/s10052-011-1554-0`].

[70] A. L. Read, "Presentation of search results: the CL$_s$ technique", *J. Phys. G* **28** (2002) 2693, `doi:10.1088/0954-3899/28/10/313`.

[71] T. Junk, "Confidence level computation for combining searches with small statistics", *Nucl. Instrum. Meth. A* **434** (1999) 435, `doi:10.1016/S0168-9002(99)00498-2`, `arXiv:hep-ex/9902006`.

[72] CMS Collaboration, "The CMS statistical analysis and combination tool: COMBINE", 2024. `arXiv:2404.06614`. Accepted by *Comput. Softw. Big Sci.*

[73] W. Verkerke and D. P. Kirkby, "The RooFit toolkit for data modeling", *eConf* **C0303241** (2003) MOLT007, `arXiv:physics/0306116`.

[74] L. Moneta et al., "The RooStats Project", *PoS* **ACAT2010** (2010) 057, `doi:10.22323/1.093.0057`, `arXiv:1009.1003`.